

WAKE INTERACTION OF A RECTANGULAR PRISM BEHIND A GEOMETRICALLY ACCURATE POROUS BARRIER

Marijo Telenta, Jožef Duhovnik, Franc Kosel, Viktor Šajin

Original scientific paper

Vortex wake interaction of a rectangular prism is numerically investigated. The wind barrier is accurately geometrically represented with a three-dimensional model in the numerical simulation. The barrier model consists of horizontal bars with different inclination angles. The unsteady Reynolds-averaged Navier-Stokes (URANS) computation is applied because the flow is not statistically stationary. The shear stress transport (SST) $k-\omega$ turbulence model is used because it shows good behavior in adverse and separated flows. Experimental study is performed to confirm the numerical data. The aim is to enhance the present level of understanding regarding bluff body wake interference flow and analyze the barrier's bar inclination effect on the sheltered object. As the bar inclination angle decreases, the bleed flow gets stronger, which results in a smaller reduction of the drag imposed on the sheltered object. The turbulent structures between the barrier and the sheltered object decrease as the bar inclination angle decreases.

Keywords: porous wind barrier, accurate three-dimensional barrier model, wake interaction, bar inclination angle

Interakcija vodenog traga pravokutne prizme iza geometrijski točno pretstavljene porozne pregrade

Izvorni znanstveni članak

Numerički je ispitivana interakcija turbulentnog traga pravokutne prizme. Vrtložna pregrada točno je geometrijski predstavljena trodimenzijskim modelom u numeričkoj simulaciji. Model pregrade sastoji se od horizontalnih profila s različitim kutovima nagiba. Primijenjen je nestacionarni Reynolds-uprosječen Navier-Stokes (URANS) proračun jer strujanje nije statistički nepromjenjivo. Rabljen je $k-\omega$ model turbulencije prijenosa smičnog naprežanja (SST) jer se dobro ponaša u suprotnim i odvojenim strujanjima. Provedeno je eksperimentalno ispitivanje kako bi se potvrdili numerički podaci. Cilj je povećati postojeću razinu razumijevanja ometanja toka vodenog traga strmog tijela te analizirati djelovanje nagiba profila pregrade na zaklonjeni objekt. Kako se smanjuje nagibni kut profila tako se pojačava strujanje zraka što rezultira manjim smanjenjem otpora nametnutog zaklonjenom objektu. Turbulencije između pregrade i zaklonjenog objekta smanjuju se kako se smanjuje kut nagiba profila.

Ključne riječi: porozna vrtložna pregrada, točni trodimenzijski model ograde, interakcija vodenog traga, nagibni kut profila

1 Introduction

Wind barriers are artificial devices used to provide shelter in various applications. The shelter effect is created by reducing the wind velocity within a certain distance behind the barrier. Wake created behind the surface-mounted vertical porous barrier involves complex phenomena. The wake consists of separations, vortex shedding, pressure gradients and high turbulent intensities. The flow around the barrier and the sheltered object is spatially and temporally complex. The barrier produces strong vortices in the wake which generates fluctuating forces on the barrier and the sheltered object. Predicting the airflow about the barrier is necessary for quantification of the barrier effects. Lack of the numerical research to investigate and explain airflow near geometrically accurate wind barriers makes optimum barrier design difficult for practical application. Optimum barrier configuration is determined by the defined barrier purpose.

The flow behind porous barrier was experimentally and numerically investigated by many researchers. The experimental studies examined a range of porosities, mainly perforated barriers, with and without sheltered objects. The Bradley-Mulhearn experiment [1] gave detailed measurements from full-scale field trials for a 50 % porous barrier with vertical bars. In the paper [2], velocity and turbulent fields behind a porous fence were measured using particle tracking velocimetry (PTV). Shelter effect of a porous barrier on triangular prism was experimentally investigated in [3]. The focus of the present research is a flow around rectangular prism behind porous barrier with horizontal bars.

Previous numerical studies modeled fluid flow through complex geometries but excluded the details of the barrier geometry. The numerical simulations were based on the Reynolds-averaged Navier-Stokes (RANS) equations with different turbulence models. In the work of [4], the barrier was modeled as a momentum extraction in the momentum equation. The $k-\varepsilon$ closure scheme gave slightly less satisfactory results than the Reynolds-stress scheme. Wind tunnel data were compared with numerical models of two-dimensional porous barrier in [5]. Two turbulence models were used, $k-\varepsilon$ and Reynolds stress. A new method was developed for determining the porous barrier resistance. Optimum barrier porosity was defined utilizing RANS simulations with $k-\varepsilon$ turbulence models in [6]. The physical effect of the porous barrier inside the flow was represented by a pressure drop through the barrier creating a momentum sink. A link between the resistance coefficient of the porous medium and the barrier porosity was made for modeling purposes. Researchers used the drag law to represent the porous effects to lower the computational cost. In this approach only the spatial average flow is represented around the barrier using the drag law. In addition, drag coefficients need to be calculated. However, little drag data of porous barriers is available.

There are considerable challenges in modeling separated flow around the object behind the porous barrier. Previous studies modeled fluid flow through porous geometries but did not consider the details of the geometry. The main focus was to define a suitable resistance model for a given geometry of a barrier. Turbulent structures in the barrier's wake need to be investigated in detail to evaluate the sheltering effect on

the object behind the barrier. Earlier studies used the Reynolds averaging method in which the porous barrier was represented as a momentum sink. In [7] was stated that numerical methods utilizing the momentum sink approach treat complex flow at a superficial level.

Former work on the wake interference in the flow around bluff bodies was mainly about cylinders in tandem. In [8] and [9] cylinder center to center distance was varied continuously and analyzed its impact on aerodynamic forces. In the work [3] shelter effect of porous wind barrier on a triangular prism was experimentally investigated. In [10] numerical study was conducted on the flow characteristics around a two-dimensional triangle behind a porous wind barrier.

The present work extends the understanding of three-dimensional bluff body near wakes and their effect on the pressure distribution on the sheltered body. This paper investigates the flow associated with the interaction of a vortex-wake with a sharp edged bluff body. Flow visualization was used to explain some of the physics associated with wake interference flow. The main objective of this study is to numerically investigate the bar inclination angle effect on the flow around the sheltered object. Optimum barrier configuration is found according to the forces acting on the sheltered object.

2 Experimental methods

The experimental study was conducted in a scaled wind tunnel simulation. Wind tunnel test section dimensions were $0,355 \times 0,407 \times 1$ m. The barrier model was built of horizontal aluminum bars. The height and length of the bars were 20 mm and 327 mm, respectively. The barrier height was $H = 145$ mm. Rectangular prism was situated behind the barrier relative to the wind direction, Fig. 1.

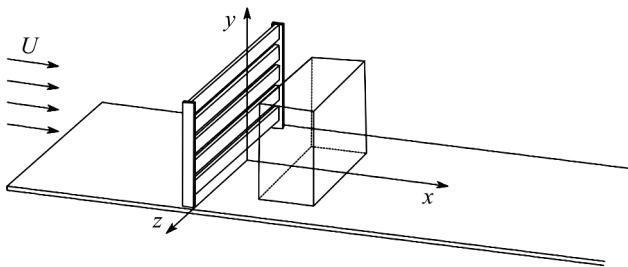


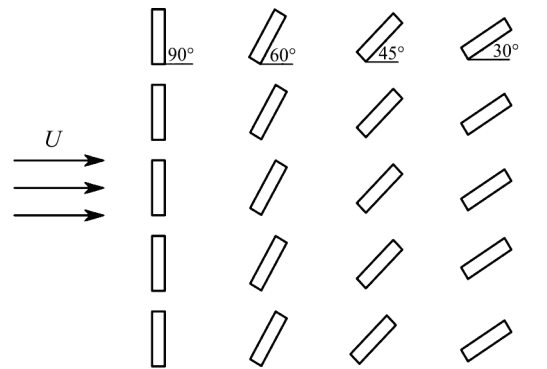
Figure 1 Barrier and sheltered object with the coordinate system

The prism dimensions were $0,625 \cdot H \times 1,25 \cdot H \times 0,95 \cdot H$. Prism center plane was placed H length from the barrier. In addition, prism was situated $0,075 \cdot H$ above the ground. No roughness elements were placed upstream of the test section to create a boundary layer. The free-stream velocity was measured with Pitot tube and it was 20 m/s. In this case, the flow was laminar with low free-stream turbulence and the prism's shape was such that all the separation locations were geometrically determined. Thus, there was little dependence on the Reynolds number. Corresponding Reynolds number based on the barrier height was $1,62 \cdot e^{-0,5}$. The stream-wise velocity profiles obtained were nearly flat. The barrier model was located in a uniform flow whose boundary layer thickness at the barrier location was approximately $0,02 \cdot H$. The

barrier model was positioned at $2 \cdot H$ downstream of the inlet test section. The drag force value was measured.

2.1 Barrier model

Solid and porous barriers can be found in use. Porous barriers are mainly used for practical applications. There are a variety of porous barrier constructions, such as upright, horizontal, screened, etc. Upright and horizontal wind barriers are usually made from bars and are widely used. The bars can be easily replaced thus this barrier type represents an economical choice. In this paper, four barrier models with different bar inclination angles are used. The inclination angles are 90° , 60° , 45° , and 30° relative to the horizontal axis for barrier configuration 1, 2, 3, and 4, respectively, Fig. 2.



Incl. angle 90° Incl. angle 60° Incl. angle 45° Incl. angle 30°
Figure 2 Wind barrier configurations

3 Numerical simulation

3.1 Solver

The numerical simulation was set to represent the scaled wind tunnel experiment. The commercial CFD code ANSYS Fluent 14.5 was utilized. ANSYS Fluent is general-purpose and standard flow solver. It uses cell-centered, in this simulation, a segregated approach, on a collocated, unstructured grid. The three-dimensional finite volume method was used for RANS equation discretization. The second-order accurate central discretization for the diffusion terms, the second-order accurate upwind discretization for the advection terms, and the second order accurate time discretization were used. The PISO algorithm was applied for pressure-velocity coupling. The results presented, unless otherwise stated, are obtained by time-averaging the unsteady simulation. A large initial transient is considered to allow the flow to develop in a quasi-steady flow.

3.2 Grid

Numerical grid was created with commercial software ANSYS ICEM-CFD. Tetrahedral grids were created due to the geometric complexity, Fig. 3. Prism layers were used near the wall boundary condition of the wind tunnel, the barrier and the prism. Strong clustering was applied close to the wall boundary conditions to capture the near-wall turbulent regions. The height of the first cell corresponds to the recommendations for the y^+ value for the turbulence model applied in the numerical

simulation. The near wall resolution was below the required 1 wall unit in the wall-normal direction. The stretching ratio between two adjacent cells was approximately 1,15.

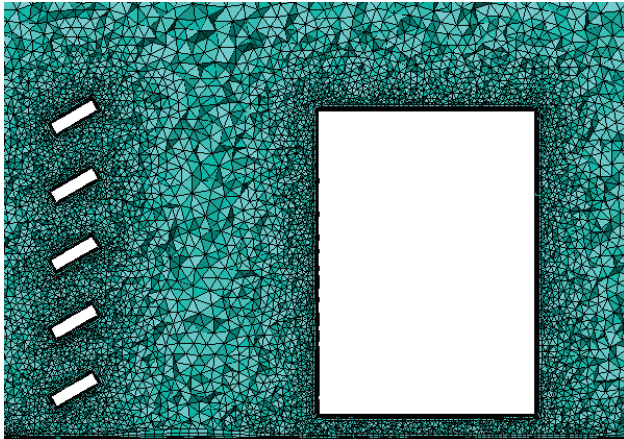


Figure 3 View of the computational grid with details of the barrier and sheltered object

3.3 Boundary conditions

Dimensions of the computational domain were set to simulate the wind tunnel and are shown in Fig. 4. The inlet was placed $3 \cdot H$ upstream of the barrier, and the flow outlet was placed $14 \cdot H$ downstream. The wind tunnel height was 0,407 m. Solid walls were used to simulate the barrier's surface and the floor, roof, and lateral walls of the wind tunnel. No-slip boundary conditions were applied on all these surfaces. Thus, the appropriate boundary layer and blockage ratio were used in the wind tunnel cross section. At the domain inflow, the upstream face, a velocity inlet boundary condition with a uniform velocity profile was specified. A small turbulence intensity of 0,1 % was imposed at the inlet corresponding to the experimental case. A pressure outlet was applied at the domain outflow. The domain was at a distance of H from the beginning of the wind tunnel walls. There, the symmetry boundary condition was applied on all sides to correctly simulate flow at the leading edge.

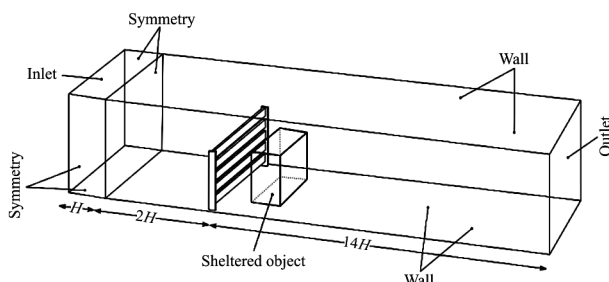


Figure 4 Extension of the computational domain and boundary conditions

3.4 Convergence criteria

Computations were calculated until the maximum continuity residual dropped five orders of magnitude. Also, the rectangular prism drag force was monitored during the iterative numerical procedure. The simulation was run until the transient flow field became statistically steady. The time step size was $2,4 \cdot e^{-0,5}$ s for configuration

1 and 2, and $1,3 \cdot e^{-0,5}$ for configuration 3 and 4. The ANSYS Fluent temporal formulation was fully implicit. Thus, there was no stability criterion that needed to be met in determining the size of the time step. The choice of the size of the time step was based on the number of iterations at each time step. The number of iterations per time step was around the recommended from 5 to 10. In addition, there were much more than the suggested 20 time steps per period for vortex shedding. A smaller time step size did not alter the numerical results.

3.5 Turbulence modeling

The governing equations due to the Reynolds averaging procedure have additional unknown variables, known as Reynolds stresses. Thus, the governing equations need a turbulence model to be solved. The turbulence model used is the shear stress transport (SST) $k-\omega$. The $k-\omega$ model is a two-equation eddy-viscosity model where the Reynolds stresses are linearly related to the mean velocity gradient (Boussinesq hypothesis) through an eddy-viscosity coefficient. Two additional transport equations have to be solved, one for the turbulence kinetic energy Eq. (1) and one for the specific dissipation energy Eq. (2), to compute the local values of the eddy viscosity.

Transport equation for turbulence kinetic energy:

$$\frac{\partial}{\partial t}(\rho k) + \frac{\partial}{\partial x_i}(\rho k u_i) = \frac{\partial}{\partial x_j} \left(\Gamma_k \frac{\partial k}{\partial x_j} \right) + \tilde{G}_k + Y_k + S_k, \quad (1)$$

Transport equation for specific dissipation:

$$\frac{\partial}{\partial t}(\rho \omega) + \frac{\partial}{\partial x_i}(\rho \omega u_i) = \frac{\partial}{\partial x_j} \left(\Gamma_\omega \frac{\partial \omega}{\partial x_j} \right) + G_\omega - Y_\omega + D_\omega + S_\omega, \quad (2)$$

where \tilde{G}_k represents generation of turbulence kinetic energy due to mean velocity gradient, G_ω is generation of specific dissipation, Γ_k and Γ_ω are effective diffusivity of k and ω , Y_k and Y_ω represent dissipation of k and ω due to turbulence, D_ω is cross-diffusion term, S_k and S_ω are user-defined source terms.

3.5.1 SST $k-\omega$ turbulence model

The SST $k-\omega$ turbulence model is a two-equation eddy-viscosity model. The main problem with the Wilcox $k-\omega$ model is its strong sensitivity to free-stream conditions. To overcome this, Menter [11] developed a model to combine the $k-\omega$ model near the surface and the $k-\epsilon$ model in the outer region. However, this model still fails to properly predict the onset and amount of flow separation from smooth surfaces. The main reason is that the model does not account for the transport of the turbulent shear stress. This results in an over-prediction of the eddy-viscosity. Proper transport behavior can be obtained by a limiter to the formulation of the eddy-viscosity:

$$v_t = \frac{a_1 k}{\max(a_1 \omega S F_2)}. \quad (3)$$

Where k is the turbulence kinematic energy, ω is the specific dissipation, F_2 is a blending function, S is an invariant measure of the strain rate, and a_1 is a coefficient.

4 Flow structure and topology

Bluff body flow field consists of three regions: the boundary layer along the bluff body, the separated free shear layer, and the wake. The boundary layer starts from the bluff body leading edge to the flow separation point. The separated shear layer starts from separating point and ends at the closure point of the recirculation zone. The shear layer is the boundary of the near wake separation bubble, consisting of recirculating flow that is at a low pressure relative to the free stream. The region behind the bluff body forms the wake. Bluff body wake dynamics has been most extensively characterized for circular cylinder. For high Reynolds numbers, the wake becomes absolutely unstable, leading to anti-symmetric shedding of vortices from the bluff body. Depending upon Reynolds number, bluff body aspect ratio, and the boundary conditions, shedding can be in line or at an oblique angle of the bluff body [12].

Flow field around two or more bodies is different from the one where body is isolated in the same flow stream. The effect of the presence of other bodies in the flow is called flow interference. Furthermore, flow interference in which body is placed behind another in relation to the free stream is called wake interference. The flow around the downstream body is unsteady and different from the free stream.

In this paper, flow around a bluff body behind a surface-mounted vertical porous barrier is considered. This flow is classified as a problem in wake interference. The wake behind the barrier is result of the recirculation flow and the bleed flow interaction. This interaction depends on the bar inclination angle.

5 Results and discussions

The flow behind the barrier presents coherent vortex shedding with a periodically oscillating wake. Coherent vortex shedding in the numerical simulation was obtained after 10 flow-through times. A time-averaged solution was computed over one flow-through time. The average drag force from the numerical simulations was compared to the one from the experimental measurements to validate the numerical simulation.

5.1 Experimental results

The experimental study was conducted to visualize the flow and to confirm the numerical data. Experimental measurements were conducted on four barrier configurations. Each barrier configuration had different bar inclination angle, that is 90° , 60° , 45° , and 30° for barrier configuration 1, 2, 3, and 4, respectively. The drag force measurements for the rectangular prism are shown in Fig. 5.

Fig. 5 shows that the drag force values decrease as the bar inclination angle increases. As one can see, the smallest drag force imposed on the sheltered object is

found for the barrier configuration with bar inclination angle of 90° .

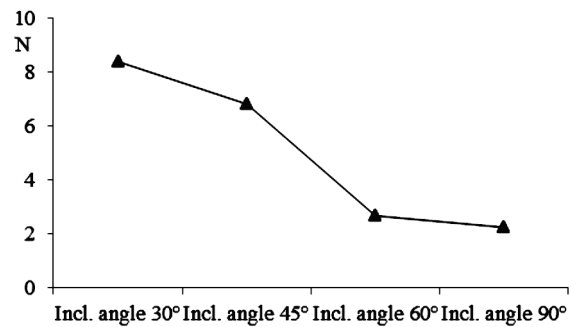


Figure 5 Experimental measurements of the drag force on the sheltered object

5.2 Grid refinement study

The discretized equations represent truncated approximations to the differential equations. The discretization error can be estimated from the difference between the solutions obtained on systematically refined and coarsened grids. The grid refinement for the grid dependency study should be substantial and systematic. It is sufficient to show the change in the computed quantity of interest for a series of grids. If the change is monotonic and the difference decreases with grid refinement, one can easily estimate where the grid-independent solution exists [13]. To investigate the discretization error, three tetrahedral grids were created for the configuration 2 wind barrier. Coarse, medium, and fine grids have 2 million, 6,8 million, and 25 million elements, respectively. The time-averaged drag force of the barrier for the three grids is shown in Fig. 6. As one can see from Fig. 6 the difference of the drag value between different grids decreases with the grid refinement and the change is monotonic. The difference of the drag forces value between the course and medium grids is 8,7 %, and difference of the drag forces value between the medium and fine grids is 2,1 %. The grid independent solution was obtained with the medium grid in the present computation.

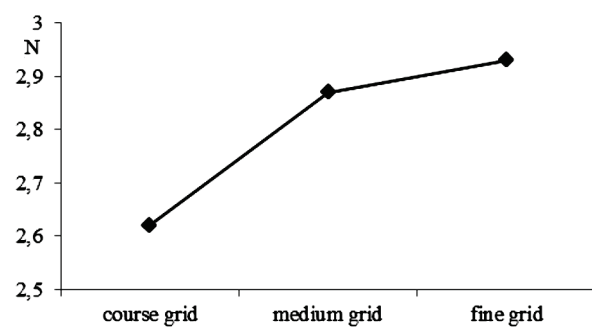


Figure 6 Grid sensitivity study for drag force value

5.3 Numerical simulation

The fluid flow around rectangular prism for the four barrier configurations was numerically simulated. The barriers have different bar inclination angles, as shown in Fig. 1. The inclination angles are 90° , 60° , 45° , and 30° relative to the horizontal axis for configurations 1, 2, 3,

and 4, respectively. The number of the grid elements was 6,8 million for each of the four cases.

Comparisons with the measurements show that the simulations agree reasonably well with the experiments in terms of the drag value. The difference between the average drag forces calculated with the tetrahedral grid and the one measured from the experiment is maximum 7 %. Hence, the results from the tetrahedral grid are considered valid for further analysis. Several possibilities may exist to account for the difference between numerical prediction and experimental results. The first may be the shortcoming of CFD or one of the modeling assumptions. The second possibility is that a slight misalignment of the barrier and the rectangular prism in the wind tunnel.

The average drag force on sheltered object calculated for the four barrier configurations with the corresponding experimental measurements is shown in Fig. 7.

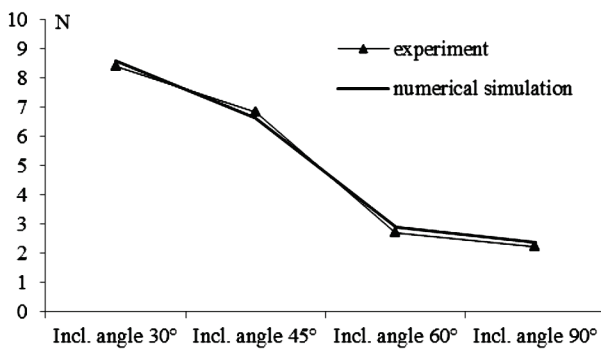


Figure 7 Comparison between the computed and measured averaged drag force on sheltered object

5.3.1 Mean pressure distribution, velocity profiles, and turbulent structures

The influence of the bleed flow and the reversed flow varies as the barrier configuration changes. The design of the wind barriers should avoid both strong bleed flow and strong reverse flow [14]. As the flow approaches the barrier, it is lifted and produces a higher velocity above the barrier. A high velocity region is formed above the barrier, resulting in a low velocity region behind it. The flow lift and velocity differ for each barrier configuration.

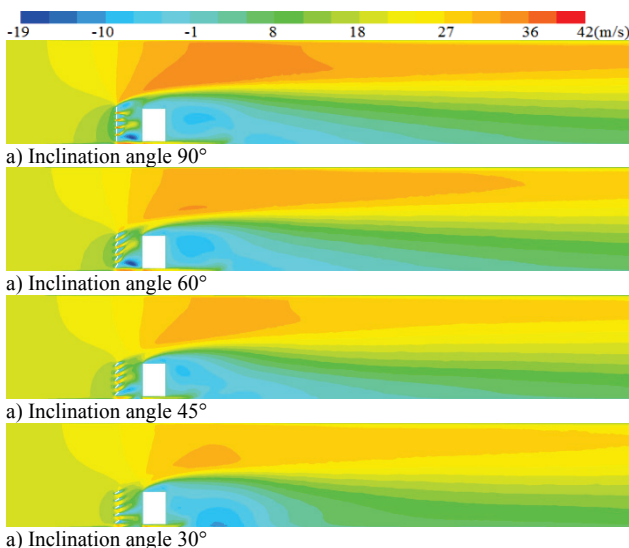


Figure 8 Contours of the mean streamwise velocity

There is a large separation cell behind the barrier with a negative wind velocity, as shown in Fig. 8. Also, there are five additional small vortices that develop immediately behind the barrier. They are a product of forward stream from the bleed flow and reversed flow from the large separation cell. The size and shape of these small areas of the reverse flow depend on the bar inclination angle. As the bar inclination angle decreases, the size of the small reversed areas decreases. The lowest vortex is the largest from the five vortices for barrier configurations 1 and 2. As the bleed flow increases, the lowest vortex weakens. Reverse cell behind the sheltered object is increasing in intensity and size as bar inclination angle decreases.

The shear layer separated from the top edge of the barrier does not interact with the sheltered object directly for the barrier configuration 1. On the other hand, the bleed flow interacts with the sheltered object for the barrier configurations 2, 3 and 4 and separation on the top part of the sheltered object occurs. Also, the bleed flow causes altered mean pressure distribution on the windward side of the object for different barrier configurations, Fig. 9. Mean pressure distribution on the windward side of the sheltered object is almost uniform for the barrier configurations 1 and 4, whereas the top part has higher mean pressure values for the barrier configurations 2 and 3. The barrier configuration 3 has higher values on a larger portion of the top side than the barrier configuration 2. Mean pressure for the barrier configuration 4 is the highest in value.

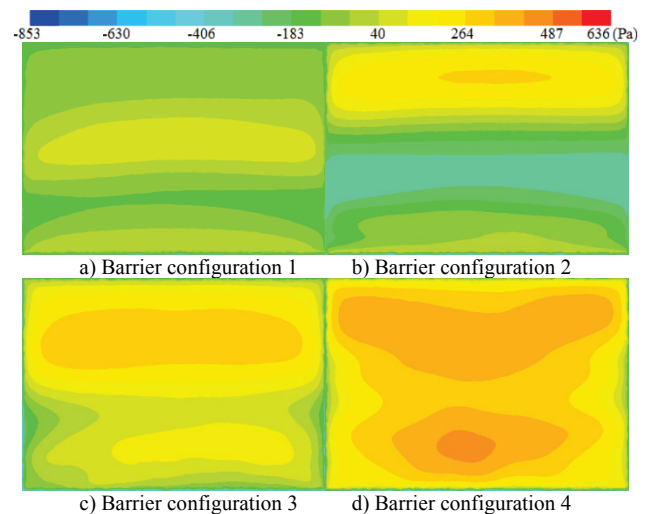


Figure 6 Mean pressure distribution on the windward side of the sheltered object

The contour plots of the turbulence kinetic energy for the four barrier configurations are shown in Fig. 10. Large turbulence kinetic energy is generated just behind the barrier for configuration 1. As the bleed flow is increasing, turbulence kinetic energy is decreasing between the barrier and the sheltered object. Exception is the barrier with bar inclination angle of 45° where turbulence kinetic energy increases in the lower position between the barrier and the shelter object. In addition, there is one large region with a high turbulence kinetic energy behind the sheltered object. The size of this region increases as the bar angle decreases.

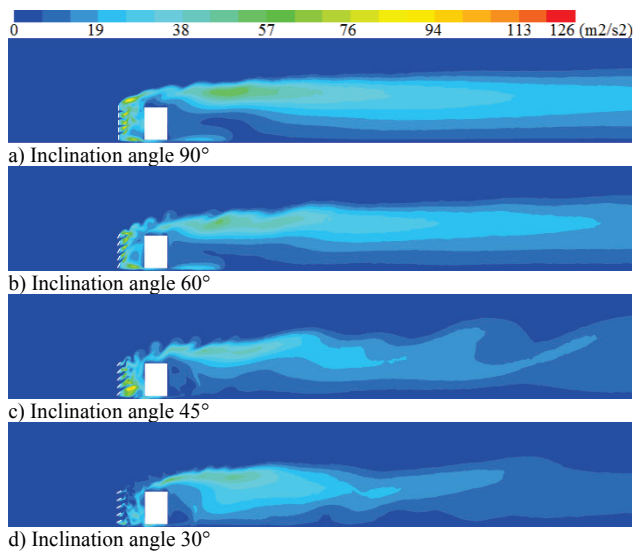


Figure 10 Contours of the turbulence kinetic energy

6 Summary and conclusion

The turbulent wake around rectangular prism behind a barrier was numerically simulated and experimentally confirmed. The wind barrier was accurately geometrically represented by a three-dimensional model. The URANS numerical simulation was utilized with the SST $k-\omega$ turbulence model. Four barrier configurations with different bar inclination angles were used in the numerical analysis. The inclination bar angles were 90°, 60°, 45°, and 30° relative to the horizontal axis.

A complex velocity field was created around the sheltered object, consisting of the bleed flow through the barrier and the reversed flow behind the barrier. The shelter effect produced by the different barrier configurations was analyzed in terms of the mean streamwise velocity component, the pressure distribution on the sheltered object, and the turbulence kinetic energy.

The main purpose of the wind barrier is to reduce the drag on the sheltered object. It is also significant to attain low turbulence in the barrier wake. The smallest drag imposed on the sheltered object is found for the barrier configuration 1. Also, for this barrier configuration pressure distribution on the windward side of the sheltered object is uniform and the smallest in the value from other barrier configurations. As the bar angle decreases, the bleed flow gets stronger, which results in a higher drag value. In addition, distribution of the pressure on the windward side of the sheltered object changes with different barrier configuration. Turbulence kinetic energy decreases between the barrier and the object as the bleed flow increases. However, turbulence kinetic energy behind the sheltered object increases with the bar inclination angle decrease. This paper relates the bar inclination angle of the barrier to the barrier shelter effect. This is achievable only if a geometrically accurate three-dimensional model of the barrier is studied.

7 References

[1] Bradley, E.; Mulhearn, P. Development of velocity and shear stress distributions in the wake of a porous shelter fence. // *Journal of Wind Engineering and Industrial Aerodynamics*. 15, 1-3(1983) pp. 145-156.

- [2] Lee, S. J.; Kim, H.-B. Laboratory measurements of velocity and turbulence field behind porous fences. // *Journal of Wind Engineering and Industrial Aerodynamics*. 80, 3(1999), pp. 311-326.
- [3] Lee, S. J.; Kim, H.-B. Velocity field measurements of flow around a triangular prism behind a porous fence. // *Journal of Wind Engineering and Industrial Aerodynamics*. 77&78, (1998), pp. 521-530.
- [4] Wilson J. D. Numerical studies of flow through a windbreak. // *Journal of Wind Engineering and Industrial Aerodynamics*. 21, (1985), pp. 119-154.
- [5] Packwood, A. Flow through porous fences in thick boundary layers: comparisons between laboratory and numerical experiments. // *Journal of Wind Engineering and Industrial Aerodynamics*. 88, 1(2000), pp. 75-90.
- [6] Santiago, J.L.; Martin F.; Cuerva A.; Bezdeneznykh N.; Sanz-Andres A. Experimental and numerical study of wind flow behind windbreaks. // *Atmospheric Environment*. 41, 30(2007), pp. 6406-6420.
- [7] Bourdin, P. & Wilson, J. D. Windbreak aerodynamics: Is Computational Fluid Dynamics Reliable? // *Boundary-Layer Meteorology*. 126, 2(2008), pp. 181-208.
- [8] Zdravkovich, M. Review of flow interference between two circular cylinders in various arrangements. // *Journal of Fluids Engineering*. 99, 4(1987), pp. 618-631.
- [9] Papaionnou, G. V.; Yue, D.; Triantafyllou, M.; Karniadakis, G. Three-dimensionality effects in flow around two tandem cylinders. // *Journal of Fluid Mechanics*. 558, (2006), pp. 387-413.
- [10] Kim, H.-B.; Lee, S.-J. Hole diameter effect on flow characteristics of wake behind porous fences having the same porosity. // *Fluid Dynamics Research*. 28, 6(2001), pp. 449-464.
- [11] Menter, F. R. Two-Equation Eddy-Viscosity Turbulence Models for Engineering Applications. // *AIAA Journal*. 32, 8(1994), pp. 1598-1605.
- [12] Shanbhogue, S. J.; Husain, S.; Lieuwen, T. Lean blowoff of bluff body stabilized flames: Scaling and dynamics. // *Progress in Energy and Combustion Science*. 35, (2009), pp. 98-120.
- [13] Ferziger, J. H.; Peric, M. *Computational Methods for Fluid Dynamics* / Springer-Verlag, Berlin, 1999.
- [14] Dong, Z.; Luo, W.; Qian, G.; Wang, H. A wind tunnel simulation of the mean velocity fields behind upright porous fence. // *Agricultural and Forest Meteorology*, 146, 1-2(2007), pp. 82-93.

Authors' addresses

Marijo Telenta, PhD candidate

Faculty of Mechanical Engineering, University of Ljubljana
 Aškerčeva 6, Ljubljana, Slovenia
 E-mail: telenta@lecad.si

Jožef Duhovnik, Prof. PhD

Faculty of Mechanical Engineering, University of Ljubljana
 Aškerčeva 6, Ljubljana, Slovenia
 E-mail: joze.duhovnik@lecad.fs.uni-lj.si

Franc Kosel, Prof. PhD

Faculty of Mechanical Engineering, University of Ljubljana
 Aškerčeva 6, Ljubljana, Slovenia
 E-mail: franc.kosel@fs.uni-lj.si

Viktor Šajn, PhD

Faculty of Mechanical Engineering, University of Ljubljana
 Aškerčeva 6, Ljubljana, Slovenia
 E-mail: Viktor.Sajn@fs.uni-lj.si